ACSNANO

www.acsnano.org

ARTICLE

Doping Graphene with Substitutional Mn

Pin-Cheng Lin,◆ Renan Villarreal,*,◆ Simona Achilli, Harsh Bana, Maya N. Nair, Antonio Tejeda, Ken Verguts, Stefan De Gendt, Manuel Auge, Hans Hofsäss, Steven De Feyter, Giovanni Di Santo, Luca Petaccia, Steven Brems, Guido Fratesi, and Lino M. C. Pereira*

Cite This: *ACS Nano* 2021, 15, 5449–5458

Read Online

ACCESS | Metrics & More | Article Recommendations | Supporting Information

ABSTRACT: **We report the incorporation of substitutional Mn atoms in high-quality, epitaxial graphene on Cu(111), using ultralow-energy ion implantation. We characterize in detail the atomic structure of substitutional Mn in a single carbon vacancy and quantify its concentration. In particular, we are able to determine the position of substitutional Mn atoms with respect to the Moiré superstructure (*i.e.*, local graphene-Cu stacking symmetry) and to the carbon sublattice; in the out-of-plane direction, substitutional Mn atoms are found to be slightly displaced toward the Cu surface, that is, effectively underneath the graphene layer. Regarding electronic properties, we show that graphene doped with substitutional Mn to a concentration of the order of 0.04%, with negligible structural disorder (other than the Mn substitution), retains the Dirac-like band structure of pristine graphene on Cu(111), making it an ideal system in which to study the interplay between local magnetic moments and Dirac electrons. Our work also establishes that ultralow-energy ion implantation is suited for substitutional magnetic doping of graphene. Given the flexibility, reproducibility, and scalability inherent to ion implantation, our work creates numerous opportunities for research on magnetic functionalization of graphene and other two-dimensional materials.**

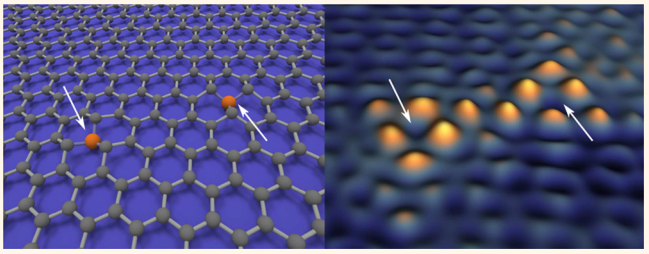

KEYWORDS: *graphene, doping, manganese, electronic structure, magnetism, ion implantation*

Magnetic functionalization of graphene is being intensively investigated for its fundamental appeal as well as for applications in next-generation electronics.[1−8] The formation of local magnetic moments and their interactions in graphene, which is intrinsically diamagnetic and exhibits electronic behavior beyond that of conventional metals and semiconductors, remains poorly understood. Harnessing such magnetic properties would enable various applications in spintronics and related technologies.

So far, magnetic functionalization of two-dimensional (2D) materials has been explored by introducing magnetic moments in different forms, including intrinsic defects such as C vacancies,[1] hydrogenation,[2] adatoms (*e.g.*, transition metals[3,9,10] and rare earths[4]), proximity to full magnetic layers,[5] and magnetic molecules.[6] However, these approaches present various limitations in terms of stability against ambient temperature and atmosphere (*e.g.*, segregation and oxidation) and of scalable device fabrication, which constitute major difficulties not only in an application scenario but also for basic research. Substitutional doping,[11,12] on the other hand, offers high stability thanks to the covalent bonding between the dopant atom and the surrounding carbon atoms in graphene.

Substitutional doping with nonmagnetic elements such as N and B can be achieved with relatively simple processes, even during growth.[13,14] Substitutional doping with typical impurities such as Si (present during growth or processing) has also been observed.[15−17] However, substitutional incorporation of magnetic elements such as transition metals is generally not thermodynamically favored due to their different chemical nature compared to C. Substitutional doping with transition elements[11,12,18] has been achieved using non-equilibrium conditions: First, vacancies are formed by bombardment with electrons or ions, and subsequently, the magnetic dopant atoms are deposited, filling the vacancies that have not dynamically annealed between the two steps. Such dual-step processes are difficult to control, especially given the complex dynamics of vacancies in graphene, thus strongly limiting their reliability, reproducibility, and scalability. Ultra-low-energy (ULE) ion implantation has the potential to overcome these limitations and has been successfully applied

Received: January 6, 2021
Accepted: February 12, 2021
Published: February 17, 2021

https://dx.doi.org/10.1021/acsnano.1c00139
ACS Nano 2021, 15, 5449−5458

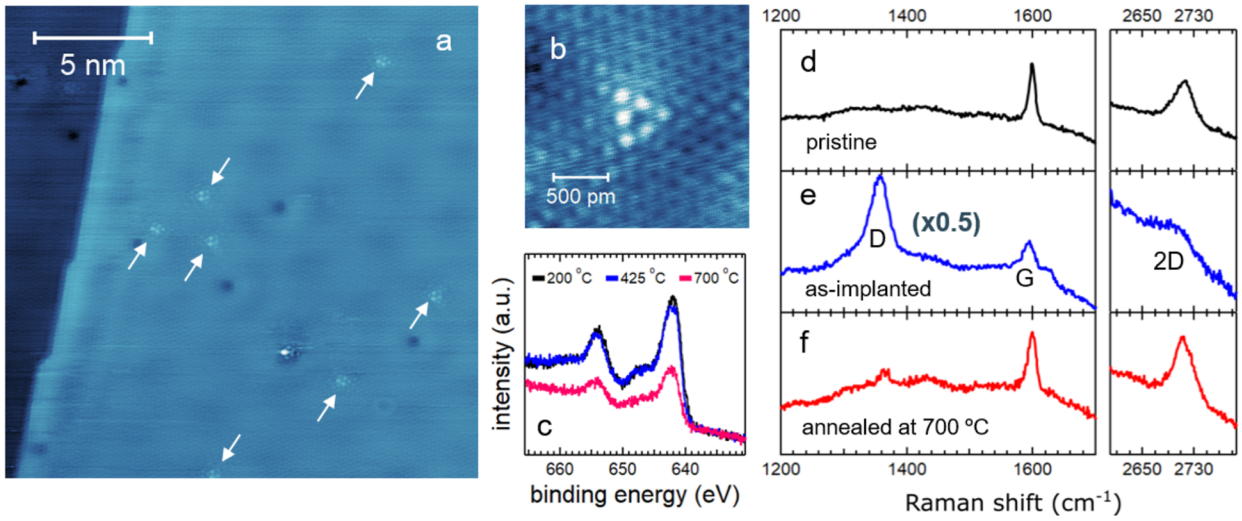

Figure 1. STM micrographs of Mn implanted graphene on Cu(111) after 700 °C annealing: (a) Large-scale micrograph showing substitutional Mn defects pointed by white arrows (V_{sample} = 200 mV, $I_{tun.}$ = 300 pA) and (b) small-scale micrograph showing one substitutional Mn defect (V_{sample} = −100 mV, $I_{tun.}$ = 5 nA). (c) Mn 2p core-level spectrum of Mn implanted graphene/Cu(111), annealed at the following temperatures after implantation: 200 °C (black), 425 °C (blue), and 700 °C (pink). (d−f) Raman spectra (laser wavelength = 532 nm) on graphene/Cu(111): (d) pristine sample annealed at 700 °C; (e) Mn implanted, in the as-implanted state; and (f) Mn implanted and annealed at 700 °C after implantation. The positions of the D, G, and 2D bands of graphene are indicated in panel (e).

to the substitutional doping of graphene with N and B,[19−23] P,[24] and Ge.[25]

Here, we report the incorporation of substitutional Mn atoms in graphene using ULE ion implantation. We selected Mn as a model case of magnetic doping, since it is expected to exhibit the largest magnetic moment among 3d transition metals in a single C vacancy,[26] which is typically advantageous for magnetic functionality. We provide a detailed characterization of the atomic structure of substitutional Mn in graphene, based on scanning tunneling microscopy (STM) and density functional theory (DFT) calculations. Furthermore, using angle-resolved photoemission spectroscopy (ARPES), we show that graphene doped with substitutional Mn retains the Dirac-like behavior of pristine graphene. These findings motivate further research on magnetic functionalization of 2D materials, strongly benefiting from the high stability of substitutional doping, together with the high degree of control, flexibility, and scalability of ULE ion implantation.

RESULTS AND DISCUSSION

Sample Preparation and Basic Characterization. The samples consist of epitaxial graphene grown by chemical vapor deposition (CVD) on epitaxial Cu(111) thin films grown on sapphire(0001) substrates, as described in ref 27. ULE ion implantation was performed by electrostatic deceleration of a $^{55}Mn^{+}$ ion beam from 30 keV to 40 eV, with perpendicular incidence with respect to the sample surface, to a fluence of 1.5 × 10^{14} ions per cm^2 (fluence rate of 1.7 × 10^{11} $cm^{-2}·s^{-1}$), measured by integration of the electric current on sample during implantation.[19,21,22] The samples were subsequently studied in the as-implanted state as well as after thermal annealing under ultrahigh-vacuum (UHV) (below 10^{-9} mbar) up to 700 °C (20 min). This article focuses on the 700 °C annealed state, where STM measurements provide the clearest identification (compared to the other annealing stages) of Mn defects that, according to the analysis described in the following paragraph, we identify as substitutional Mn atoms in graphene. Moreover, this STM-based identification allows us to quantify its concentration as 0.04 ± 0.02% with respect to C atoms in graphene (Figure 1a,b and Table S1), which corresponds to approximately 1% of the implanted ions (*i.e.*, 1% of the implanted 1.5 × 10^{14} ions per cm^2) being substitutionally incorporated. The remainder corresponds to Mn ions in other configurations: backscattered during implantation (*i.e.*, back into the vacuum upon collision with C and Cu atoms), adsorbed onto graphene, intercalated between graphene and the Cu surface, or diffused into Cu upon annealing. Nonsubstitutional configurations are also observed in the STM data, although not as clearly identified (Figure S3). Synchrotron X-ray photoelectron spectroscopy (XPS) measurements reveal a decrease in Mn concentration (with respect to C in the graphene layer) upon annealing: from 2.3% and 2.2% after thermal annealing at 200 and 425 °C, respectively, to 1.0% after annealing at 700 °C (Figure 1c; additional details are given in Supporting Information). We did not determine the Mn concentration in the as-implanted state, that is, as-mounted in the UHV chamber after exposure to ambient conditions, since in that state, the surface is inherently highly contaminated, hindering quantification and possibly modifying the sample surface upon photon irradiation (more details in Supporting Information). The Mn concentration at low annealing temperature (2.3% for at 200 °C) corresponds to about half of the Mn fluence (1.5 × 10^{14} cm^{-2}), indicating that approximately half of the implanted ions are in fact backscattered (lost to the vacuum) already during the implantation process (but still deposit their charge, thus being accounted in the fluence value). The further decrease upon annealing (down to 1% at 700 °C) can be understood as due to desorption of Mn atoms (*i.e.*, loss of Mn to the vacuum) which had initially adsorbed onto graphene during implantation and diffusion of intercalated Mn deeper into the Cu layer (*i.e.*, the Mn atoms remain in the sample, but their apparent intensity decreases due to inelastic scattering of the photoelectrons). Thermal annealing also removes adsorbed contaminants resulting from exposure to air between the multiple

https://dx.doi.org/10.1021/acsnano.1c00139
ACS Nano 2021, 15, 5449−5458

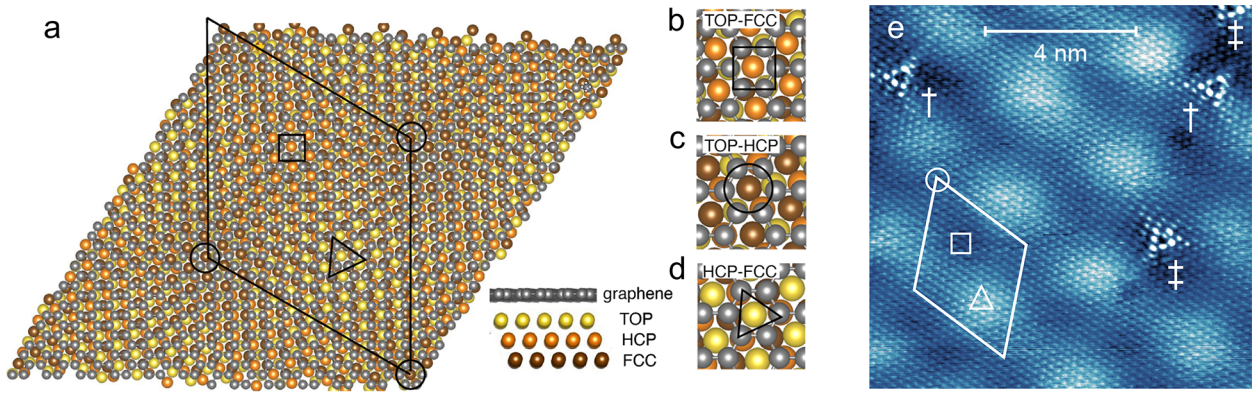

Figure 2. (a) Moiré superstructure of graphene/Cu(111), resulting from the different graphene-Cu stacking regions: (b) TOP-FCC, (c) TOP-HCP, and (d) HCP-FCC. (e) STM micrograph (V_{sample} = 100 mV, $I_{tun.}$ = 100 pA) showing the Moiré superstructure and substitutional Mn defects within them: TOP-FCC stacking with Mn on the fcc site (marked with †) and TOP-HCP stacking with Mn on the HCP site (marked with ‡). The identification of the stacking region and of Mn site is described in the main text. Symbols (○, □, △) are overlaid to link the identification of the three stacking regions in the various panels.

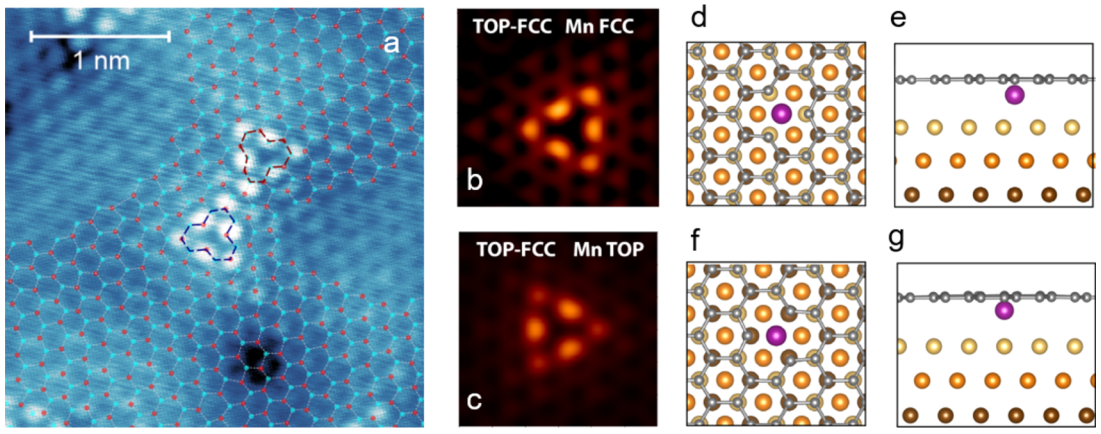

Figure 3. (a) STM micrograph (V_{sample} = −100 mV, $I_{tun.}$ = 5 nA) exhibiting two substitutional Mn defects in opposite graphene sublattices, showing triangular features which are mirror reflected with respect to each other. DFT simulated STM for substitutional Mn in a TOP-FCC stacking region (energy window [−0.25 eV, E_F]): (b) for Mn in FCC site and (c) in TOP site. Relaxed model structures obtained from DFT: (d, e) top and side views, respectively, for Mn in FCC site; and (f, g) top and side views, respectively, for Mn in TOP site.

synthesis and characterization steps (*cf.* Tables S3 and S4). Raman spectroscopy (Figure 1d–f) shows the onset of significant disorder upon implantation (Figure 1e), with the emergence of a D peak with a peak-height ratio with respect to the G peak (I_D/I_G) of 2.14, whereas in the pristine sample (Figure 1d), no D peak is observed. A low-disorder state is recovered upon annealing at 700 °C (I_D/I_G = 0.19). The residual D peak intensity is likely related to the substitutional Mn defects, although other defects (formed upon implantation or annealing) cannot be excluded. In short, the (partial) removal of nonsubstitutional Mn components, combined with a cleaner graphene surface and low disorder, make the 700 °C annealed state particularly suitable for a more detailed study of substitutionally doped graphene, which constitutes the remainder of this article.

Atomic-Scale Structure of Substitutional Mn. By combining STM measurements and DFT simulations, we are able to analyze the atomic-scale structure of substitutional Mn in extreme detail. In the following, we present the main findings regarding the identification and structure of the defects. Further details are given in Supporting Information. We must first consider the stacking between the graphene lattice and the Cu(111) surface. As a result of the different lattice parameters (2.46 Å for graphene and 2.56 Å for the Cu surface) and of the angular orientation of graphene with respect to the Cu surface (±3.57°, determined using low-energy electron diffraction, *cf.* Figure S6b), the graphene-Cu stacking varies continuously across the surface (Figure 2a) leading to a Moiré superstructure (Figure 2e). Three points with high-symmetry stacking can be defined indicating the position of the two C atoms in the graphene unit cell with respect to the underlying substrate: TOP-FCC, TOP-HCP, and HCP-FCC (Figure 2b–d, respectively). Between these points, the stacking has a lower symmetry. These high-symmetry points define a periodic 2D lattice, which is observed in the STM topographies as a Moiré superstructure (Figure 2e). The identification of the three high-symmetry stacking regions in the STM topographies (Figure 2e) is based on the simulated Cu-graphene distances (2.60 Å for TOP-FCC, 2.70 Å for TOP-HCP, and 2.87 Å for HCP-FCC), which is reflected in the STM data as height differences, that is, lowest for TOP-FCC and highest for HCP-FCC (Figure S7). For a given high-symmetry stacking, and assuming that only one C vacancy is available, Mn can substitute for one of two nonequivalent C atoms. For example, for TOP-FCC stacking, Mn can substitute for the C atom that is vertically aligned

https://dx.doi.org/10.1021/acsnano.1c00139
ACS Nano 2021, 15, 5449–5458

either with the TOP site or the FCC site of the Cu surface (Figure 3). We performed DFT calculations for all six combinations of three stackings and two sites.

Furthermore, by comparing DFT-simulated and experimental STM topographies, we identify the surface structure of Mn substituting for a single C atom, that is, located at a single C vacancy (Figure 3). This unambiguous identification is based not only on the comparison to simulations of substitutional Mn in a single vacancy but also to simulations of a wide range of other defects, intrinsic or Mn-related: free single vacancies, free double vacancies, Mn in double vacancies, and intercalated Mn (without vacancy), all of which can be distinguished from substitutional Mn in a single vacancy (Figure S1). Some of these other defects are indeed observed in our samples (Figure S3), although their identification is more ambiguous than that of substitutional Mn, which is the focus of the present article. We also note that we observe substitutional Mn defects already in the as-implanted state; however, as mentioned above, given the cleaner surface and lower degree of disorder, here we focus on the 700 °C annealed state. For all the six analyzed substitutional configurations, we find that the STM simulations reproduce the shape and contrast observed in the STM measurements. The TOP-FCC case is illustrated in Figure 3; additional simulations are shown in Figure S2. By referring to our structural model (Figure 3d−g), we are able to identify the six protrusions producing the characteristic triangular symmetry as the carbon atoms from the sublattice opposite to the vacancy sublattice (corresponding to the substitutional Mn site), with the three nearest neighbors to the substitutional Mn exhibiting the highest intensity. In contrast, the Mn site appears as a dark region, consistent with the lower position of the Mn atom with respect to the surrounding C atoms. In Figure 3a, we exhibit in particular two substitutional Mn defects in opposite graphene sublattices, showing triangular features which are mirror reflected with respect to each other, again in agreement with the symmetry relation obtained in the DFT simulations (Figure 3b,c). The site identification of the Mn defects in Figure 2e is based on this relation between stacking region, Mn site (*i.e.*, C sublattice), and orientation of the triangular-shaped objects in the STM data; no other differences were observed in the topographic signatures for substitutional Mn in different stacking regions.

A particularly important aspect of the atomic structure of substitutional Mn is the vertical displacement with respect to the graphene layer (Figure 3e,g). Due to the short bond lengths that characterize graphene and to the large effective radius of Mn compared to the free space left by the vacancy, substitutional Mn atoms relax away from the graphene plane (Figure 3e,g). This out-of-plane displacement has been proposed to occur for various substitutional dopants in graphene (*e.g.*, P).[24] However, previous studies on such effects have focused on suspended graphene, which has mirror symmetry with respect to the graphene plane, before being broken by the out-of-plane displacements upon substitution. In the present work, the Cu substrate breaks that mirror symmetry, and we observe that Mn is displaced toward the Cu surface, while the carbon atoms surrounding the Mn atom are slightly buckled away from the Cu surface, with an overall corrugation not exceeding 0.1 Å. The Mn−Cu distance is ∼2 Å, while the equilibrium distance between the surface and the graphene layer is ∼3 Å. Interestingly, the C nearest neighbors (to Mn) do not retain, upon relaxation, the reconstruction that is typical of the single vacancy (taken as starting configuration); instead they symmetrically displace in plane in order to accommodate the substitutional Mn atom (the C−C bond distance within the same sublattice is 2.82 Å, corresponding to an increase of 11% compared to the same distance obtained far from the Mn defect). This configuration is obtained as the final (relaxed) state when starting with the Mn atom just below the graphene layer. The configuration with the Mn atom above the vacancy site (protruding outward, into the vacuum) can also be obtained as a final state of the DFT simulation, by placing the Mn atom exactly at the vacancy position and allowing for relaxation. For this final structural configuration (protruding outward), the STM simulation shows a very distinct signature: bright Mn position *versus* dark surrounding C atoms (Figure S1c), that is, the opposite of what we observe for the defects that we identify as substitutional Mn. From STM data, which is local in nature, we cannot completely exclude that the outward-protruding configuration is also present for a minority fraction of the Mn atoms (*cf.* one rare case in Figure S3a that resembles the DFT simulation in Figure S1c). Nevertheless, this outward configuration is very rare, and we only detected a few objects in all our STM data that may be associated with it, that is, more than 2 orders of magnitude lower probability compared to the inward configuration. This absence (or unlikely occurrence) of the outward configuration is consistent with our DFT calculations, yielding a higher total energy (by 2.25 eV) compared to the inward configuration (Figure 3e,g).

Electronic Properties of Graphene Doped with Substitutional Mn. Our DFT calculations yield significantly different energies for substitutional Mn in different stacking regions and sites (Table 1). For the most stable TOP-FCC stacking, the two possible sites, namely FCC and TOP, differ for 0.33 eV. A similar value is also found for the two substitutional configurations of the TOP-HCP stacking, while the site dependence is less marked in the HCP-FCC case. On the other hand, taking the same site for different stacking, we found energy differences ranging between 0.12 (TOP-site) and 0.64 eV (FCC-site). On the basis of these results, we can conclude that the substitution in TOP position is unfavored, while the FCC site is preferred, and its stability is dependent on the local stacking. We were able to clearly identify the stacking-site configuration (Figure 2e) for only a few substitutional defects, since it requires a clear imaging of the defect as well as of the Moiré superstructure (*e.g.*, Figure 2e). Although the observed trend is consistent with the calculated total energies, that is, predominance of the two lowest-energy configurations (TOP-FCC stacking with Mn in the FCC site and TOP-HCP stacking, with Mn in the HCP site), the present statistics are too low to be conclusive. Future studies

Table 1. Total Energy Difference ΔE_{tot} for Substitutional Mn in Different Stacking Site Configurations, with Respect to TOP-FCC Stacking with Mn in the FCC Site[a]

stacking	site	ΔE_{tot} (eV)	μ_{Mn} (μ_B)	μ_C (μ_B)
TOP-FCC	FCC	0.00	3.38	−0.22
TOP-FCC	TOP	0.33	3.14	−0.21
TOP-HCP	HCP	0.17	3.37	−0.22
TOP-HCP	TOP	0.45	3.15	−0.22
HCP-FCC	FCC	0.64	3.35	−0.21
HCP-FCC	HCP	0.66	3.36	−0.21

[a]For each configuration, the magnetic moment of Mn (μ_{Mn}) and of the C atoms (μ_C) surrounding the vacancy (average) is also given.

https://dx.doi.org/10.1021/acsnano.1c00139
ACS Nano 2021, 15, 5449−5458

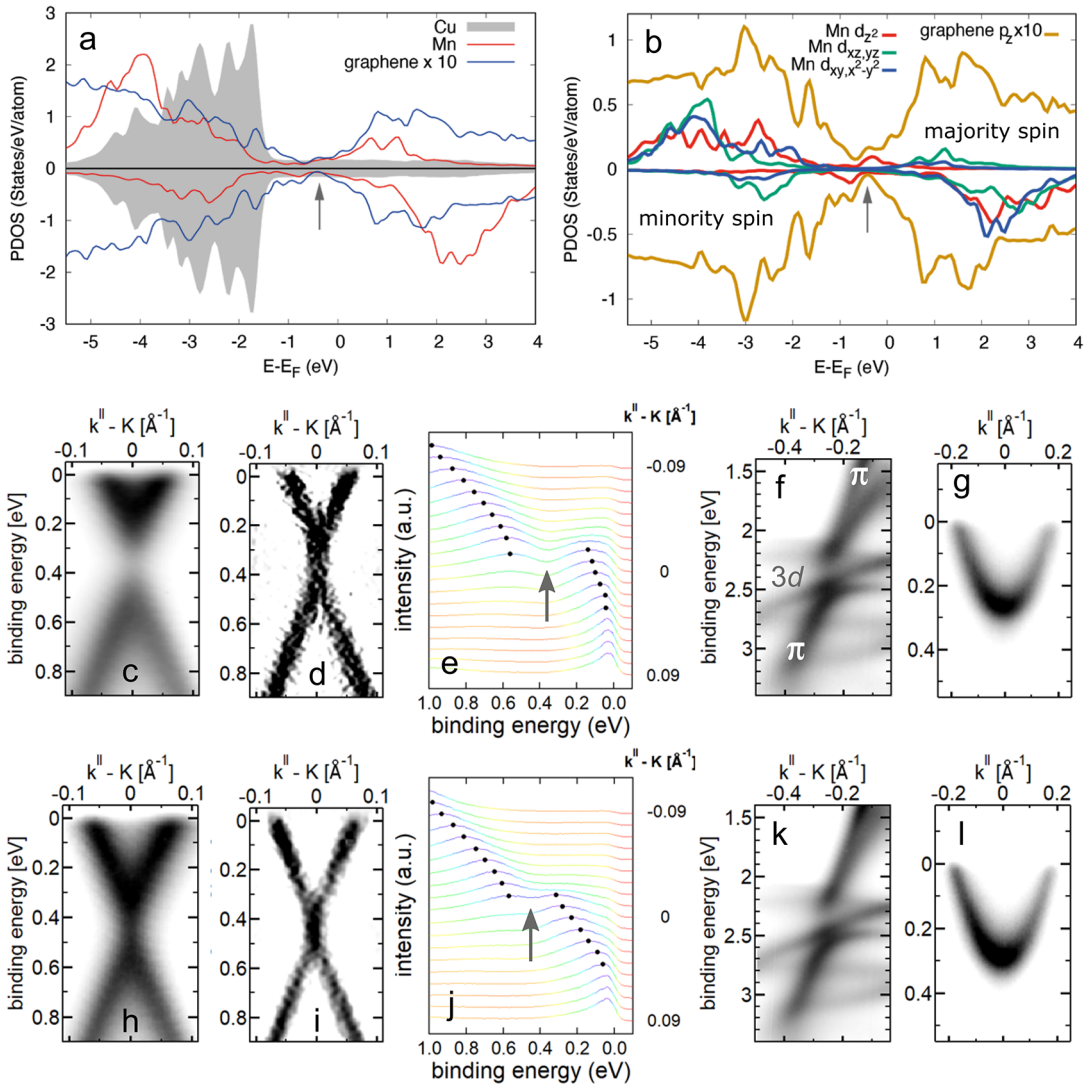

Figure 4. (a, b) Density of states (PDOS) projected on the different elements (a) as well as on the different orbital components (*i.e.*, magnetic quantum number *m*) of Mn and p_z states of graphene (b), for a substitutional Mn concentration of 1%. The majority and minority spin components are plotted as positive and negative PDOS, respectively. (c–l) ARPES spectra ($h\nu$ = 34 eV) measured after 700 °C annealing, on pristine (c–g) and Mn implanted (h–l) samples. Panels (c, h) show 2D spectra measured near the K-point along the Γ → K direction; panels (d, i) display the second derivative of the data in (c, h), highlighting the Dirac cone dispersion of the π and π* bands of graphene. (e, j) Energy distribution curves extracted from the p-polarization branch of the data in (c, h), with a wavenumber (*k*) step of 0.01 Å^{-1}. (f, k) 2D spectra measured in the region where the graphene π-band and the Cu 3d-band intersect; the observed discontinuity in the graphene π-band results from hybridization with the Cu 3d-band. (g, l) Cu(111) surface state measured at the Γ point. In panels (e, j), the dots mark the local maxima. The arrows in panels (a, b, e, j) point to the gap region, indicating that Mn d_z states emerge in (j) according to the PDOS in (a, b). In the ARPES panels (c-l), binding energy is defined as BE = $E_F - E$.

should investigate these effects in more detail. Nevertheless, our DFT calculations yield similar electronic properties for all the six simulated stacking-site configurations of substitutional Mn. The Mn atom is characterized by a reduction of electrons (−0.33 e) with respect to the ideal atomic valence. The n-doping of the graphene layer (+0.62 e) is slightly smaller than in the bare vacancy case (+0.75 e). The electrons donated by the Mn atom provide about half of the charge that is necessary for charge stability of the graphene+Mn overlayer, resulting in less charge donated by the substrate (−0.30 e) compared to the bare vacancy case (−0.75 e). The charge transfer also influences the magnetic properties of the system (Table 1), in particular in the close surrounding of the substitutional atom. We obtain calculated magnetic moments for Mn (μ_{Mn}) around 3.4 μ_B, and for the C, nearest neighbors (μ_C) around 0.2 μ_B, that is, lower in absolute value compared to the bare vacancy case (0.49 μ_B). Moreover, μ_C is antiparallel with respect to μ_{Mn} (the reason for the negative values of μ_C in Table 1).

While so far we discussed essentially local electronic properties, we now turn our attention to the effect on Mn doping on the overall electronic properties (band structure) of graphene. Our DFT calculations yield a magnetic ground state for substitutional Mn in graphene/Cu, as can be deduced from the density of states (Figure 4a,b) projected on different species (PDOS). In addition to the spin-polarized PDOS of Mn, we find a 0.15 eV shift between majority and minority spin components at the Dirac cone of graphene (Figure 4a,b and Figure S10), confirming the interaction between the Mn atom and the carbon overlayer. In particular, the PDOS resolved in orbital components shows the hybridization between d_{z^2}

https://dx.doi.org/10.1021/acsnano.1c00139
ACS Nano 2021, 15, 5449−5458

orbitals of Mn and p_z states of graphene at the Fermi level, while the states belonging to the other d components lie far from the Dirac cone. The PDOS of the substrate is not spin polarized, and no changes are visible in the d-band with respect to the clean surface, if the *k*-integrated PDOS is considered. On the other hand, the PDOS at $\bar{\Gamma}$ (not shown) exhibits a shift of the Shockley state of Cu toward lower energies with respect to graphene with a bare carbon vacancy on the same substrate, in agreement with the smaller charge transfer from the substrate to the overlayer, as discussed above. Additional details on the calculated band structure are given in Figures S9 and S10.

Figure 4c–l compares ARPES data for pristine (c–g) and Mn-implanted graphene (h–l), both after annealing at 700 °C. The first observation is that the data (measured at 80 K) do not provide a clear indication of the spin-splitting predicted by DFT (corresponding to an effective temperature of 0 K), that is, a single set of Dirac cones is observed, without indication of 0.15 eV spin-splitting predicted by DFT (Figure S10). The DOS near the Dirac point does increase as predicted for substitutional Mn (*cf.* arrows in Figure 4a,b,e,j), but finer details cannot be resolved. In fact, the ARPES measurements (Figure 4) show only a subtle effect of Mn doping in the band structure. We observe an increase in the n-doped character of the implanted sample (Figure 4c,d,h,i): The Fermi level position with respect to the Dirac point changes from 0.33(1) eV in the pristine sample to 0.43(1) eV in the implanted sample. A decrease in the band gap is also observed from 0.40(2) eV to 0.23(2) eV. Other key features are essentially unaffected: The Cu surface state (Figure 4g,l) is clearly visible, indicating that no significant oxidation of the interface has occurred;[28] the hybridization between Cu 3d and graphene π states (Figure 4f,k) is also clearly visible, indicating that the Cu-graphene coupling is not significantly affected; and no change in Fermi velocity can be resolved ($0.91(3) \times 10^6$ ms^{-1} and $0.88(4) \times 10^6$ ms^{-1} for pristine and implanted, respectively). The observed n-doping effect in the pristine sample is well understood as due to the charge transfer from the Cu surface.[29] The increase upon Mn implantation and annealing is unlikely to be a result of substitutional Mn doping, but instead an effect of the intercalated Mn component, for the following two reasons. First, our DFT calculations for substitutionally doped graphene show no increase of n-doping effect, which is instead found for intercalated Mn (Figure S9). Second, after 700 °C annealing, our STM data show intercalated objects which are likely to correspond to intercalated Mn islands (Figure S3e). Based on the understanding that charge-transfer effects in graphene-metal interface are mostly dependent on the work functions,[29] and considering that the work function of Mn [4.1(2) eV] is lower than that of Cu [4.65(5) eV],[30] we can therefore expect a measurable n-doping effect from the Mn islands. Moreover, if intercalated Mn atoms (as isolated Mn atoms) are still present after 700 °C (*i.e.*, have not segregated into islands and have not diffused in the Cu layer), they are also expected to contribute to n-doping on the basis of our DFT calculations. The band gap in the pristine sample is a well-known effect for graphene on Cu(111)[31,32] (resulting from the hybridization between Cu 3d and graphene π states), which is overestimated due to directional broadening when the ARPES beam probes multiple grains which are not perfectly aligned with respect to each other,[31] as is the present case. The apparent decrease in band gap in the Mn-doped sample is likely due to Mn DOS (mostly d_{z^2} orbitals) emerging near the Dirac point (*cf.* arrows in Figure 4a,b,e,j) and hybridizing with the p_z states of graphene, as predicted by our DFT calculations (Figure 4a,b). Indeed, in the Mn-doped case, while an energy gap can still be extracted by taking the energy difference between local DOS maxima, (arrow in Figure 4j), the DOS is nearly constant in that region, that is, there is effectively no gap. In short, the Dirac-like character of graphene is preserved upon substitutional Mn doping, with strong indication of hybridization between Mn and graphene states near the Dirac point. This makes Mn-doped graphene an ideal system in which to study strong coupling between local magnetic moments and Dirac electrons, as we discuss below in the context of future research.

Substitutional Mn Formation and Stability. There are essentially two possible paths for the formation of substitutional Mn in graphene by ULE ion implantation: (1) Direct substitution in which the impinging Mn ion displaces a C atom and takes its position, and (2) a diffusion-assisted mechanism in which an implanted Mn atom (adatom or intercalated) diffuses (in plane) and becomes trapped in a C vacancy which had been created by an arbitrary Mn ion. Both mechanisms are likely to take place in the present case, and both require the formation of a C vacancy, which by simple kinematics (conservation of kinetic energy and momentum)[33] requires a minimum initial energy of the impinging ion given by

$$E_{\min} = E_t \frac{(M_{Mn} + M_C)^2}{4 M_{Mn} M_C} \quad (1)$$

where E_t is the C threshold displacement energy (*i.e.*, minimum energy that must be transferred to the C atom to create a stable C vacancy), and M_{Mn} and M_C are the atomic mass of Mn and C, respectively. With $E_t \approx 22$ eV,[34] eq 1 gives $E_{\min} \approx 37$ eV. This minimum energy corresponds to a head-on collision (zero impact parameter). The larger the impact parameter, the smaller the transferred energy becomes, that is, Mn atoms impinging with a larger impact parameter with respect to the closest C atom must have an energy higher than 37 eV in order to still displace a C atom. We chose an implantation energy of 40 eV, that is, above the threshold of 37 eV, so that a nonvanishing fraction of the implanted Mn ions transfer sufficient energy to create a vacancy, but not too high, to minimize the Mn backscattering energy (leading to loss of Mn to the vacuum).

From our DFT calculation we can also evaluate the stability of substitutional Mn. The binding energy between an implanted Mn atom and a vacancy can be estimated as

$$E_b = (E_{Mn\text{-}sub} - E_{gr@Cu}) - (E_{vac\text{-}gr@Cu} - E_{gr@Cu}) - (E_{Mn\text{-}interc} - E_{gr@Cu}) = -5.3\text{eV} \quad (2)$$

where $E_{Mn\text{-}sub}$ and $E_{Mn\text{-}interc}$ are the total energies of the system with Mn in substitutional and intercalated positions (*i.e.*, with and without an associated carbon vacancy), $E_{gr@Cu}$ is the total energy of pristine graphene on Cu(111), and $E_{vac\text{-}gr@Cu}$ of that system with a single vacancy. Such a strong binding (−5.3 eV) confirms the tendency of the implanted Mn atoms to combine with existing vacancies in the graphene lattice as well as the high thermal stability of the substitutional configuration (at least up to 700 °C, as reported here).

While in the present case (ULE ion implantation), both direct and diffusion-assisted substitutions are likely to occur, two-step doping approaches in which the vacancy formation

https://dx.doi.org/10.1021/acsnano.1c00139
ACS Nano 2021, 15, 5449–5458

and the incorporation of transition metals (*e.g.*, Fe, Co, Ni, Mo, Pt) correspond to two separate processes[11,12,18,35] are essentially based on the diffusion-assisted mechanism. For example, vacancies are formed by electron irradiation, followed by thermal deposition of the metal atoms, which diffuse on the surface until becoming trapped in the previously formed vacancies. Diffusion-assisted substitution has been observed to be thermally activated (*i.e.*, occurring only upon annealing above room temperature).[35] This would imply that, if part of substitutional Mn in our samples was indeed formed *via* a diffusion assisted-mechanism (*i.e.*, not exclusively by direct substitution), the postimplantation annealing played a critical role. Since its atomic number is similar to Mn (Z = 25), it is interesting to further compare our results (in terms of defect structure, electronic properties, and stability) to those previously obtained for Fe (Z = 26) doping *via* two-step processes. The atomic structures of the two types of defects are similar (Mn here and Fe in ref 12, in a single C vacancy), characterized by strong relaxation effects resulting from the large effective radius of Mn/Fe compared to the C atom that they substitute: In-plane displacement of the neighboring C atoms away from the metal atom; and out-of-plane displacement of the metal atom and (although less pronounced) of the neighboring C atoms. There is, however, a difference in the latter (out-of-plane displacement), already mentioned above, resulting from the fact that in the present work, the graphene layer is supported on a substrate, while in ref 12, it is suspended. While in suspended graphene it is generally accepted that the out-of-plane displacement of the metal dopant and of neighboring C atoms occurs in the same direction, in our case, as mentioned above, the Cu substrate breaks the mirror symmetry with respect to the graphene plane. Consequently, the metal dopant (Mn) is observed to displace toward the Cu surface, whereas the neighboring C atoms are displaced away from it, resulting in a total energy that is 2.25 eV lower than for a configuration in which both the Mn and C atoms are displaced away from the Cu surface. In terms of electronic structure, there is a striking difference between substitutional Mn and Fe: While for Mn, the electrons in (different) nonbonding d orbitals add up to a local moment of approximately 3 μ_B, in Fe, the 3d spins pair up resulting in a vanishing local moment.[26] In terms of stability, the fact that we observe no signs of instability up to 700 °C supports the calculated high binding energies of metal atoms such as Mn and Fe in single C vacancies: ∼ −5 eV for substitutional Mn in graphene/Cu(111) as reported here, and ∼ −6 eV and ∼ −7 eV for Mn and Fe, respectively, in suspended graphene.[26] The fact that we do not observe signs of clustering of substitutional Mn atoms up to 700 °C is also consistent with calculated migration barriers of ∼3 eV for 3d metals.[26] As mentioned in ref 35, the lower stability observed in that work is likely a consequence of a different defect structure, that is, not an *ideal* substitution into a single C vacancy.

Future studies should evaluate the roles of direct and diffusion-assisted substitution as well as the effect of thermal annealing and varying ion energy on the substitution efficiency, in particular, toward higher substitutional concentrations. In the present work, with an implantation energy of 40 eV, the 0.04% substitutional concentration (determined from STM) corresponds to about 1% efficiency with respect to the implanted fluence. Further optimization, in particular toward slightly higher energies, is likely to further increase the substitutional efficiency, by increasing the vacancy formation rate, without significantly increasing the Mn backscattering energy. In any case, the substitutional concentration can in principle be increased by increasing the fluence. For example, a substitutional concentration of about 1% (with a substitution efficiency of a few %) was obtained with ULE ion implantation (25 eV) of nitrogen[20] (for N, eq 1 gives $E_{min} \approx 22$ eV, that is, also slightly below the implantation energy, as in the present case).

Prospects for Magnetic Functionality. As mentioned above, ARPES measurements at 80 K do not provide evidence of the spin-splitting (ferromagnetic state) predicted by DFT (corresponding to an effective temperature of 0 K). Various reasons may explain this. First, the ordering temperature may simply be below 80 K. Second, the local magnetic moment of substitutional Mn may in fact be strongly decreased or completely screened by the conduction electrons (Kondo effect, which has been reported for magnetic defects in graphene at temperatures as high as 90 K),[36] which would inhibit a ferromagnetic state. Future studies should therefore specifically address the magnetic properties of substitutionally doped graphene. On the theoretical side, more complex approaches including many-body effects related to electronic correlation can be adopted, such as the tight binding model with Hubbard term[37] or DFT + dynamical mean-field theory in the Anderson impurity model[38] which allow to describe Kondo physics. On the experimental side, various advanced techniques can be applied that provide insight at various scales, for example, local studies based on scanning tunneling microscopy and spectroscopy, including with spin-polarized capabilities;[3,8,39] macroscopic studies based on X-ray magnetic circular dichroism;[40,41] spin-resolved band structure characterization based on spin-resolved ARPES;[42] and magnetotransport studies (*e.g.*, Hall effect and magnetoresistance measurements).[36]

Magnetic Doping of 2D Materials by ULE Ion Implantation. Our approach to magnetic substitutional doping, based on ULE ion implantation, offers various advantages. For example, contrary to two-step approaches,[11,12,18] we can control both processes of vacancy creation and dopant incorporation with a single set of implantation parameters, which can be expected to yield better reproducibility. All the implantation parameters (energy, fluence, fluence rate, and temperature) can be precisely monitored and controlled, which in general provide a high degree of control and reliability. Moreover, the resulting atomic configuration, in which the Mn atom is underneath (protected by) the graphene layer, can be expected to provide more stability with respect to exposure to the atmosphere and postprocessing steps (*e.g.*, deposition of a polymer layer for transfer or of an oxide layer for top gating). The approach is also extremely flexible, being compatible with virtually any element of the periodic table (as dopant) and any 2D material (as host). Although one can expect some limitations regarding which elements can effectively be substitutionally incorporated into a given 2D material, those should be less restrictive compared to processes that occur closer to equilibrium (*e.g.*, doping during growth). Therefore, the present work motivates further research, even beyond magnetic doping of graphene, for example, magnetic doping of MoS_2 and related 2D semiconductors for spintronics and valleytronics applications[43] and creation of spin defects in h-BN and related 2D insulators for quantum technologies.[44,45] Finally, ion implantation is widely used for semiconductor processing in microelectronics;

https://dx.doi.org/10.1021/acsnano.1c00139
ACS Nano 2021, 15, 5449−5458

if ULE ion implantation technology is further developed to the level of its higher energy counterpart, one can expect it to be compatible with wafer-scale fabrication.

CONCLUSION

To conclude, we demonstrate the incorporation of substitutional Mn in graphene using ULE ion implantation and provide a detailed characterization of its local atomic structure. We also show that graphene doped with substitutional Mn retains the Dirac-like behavior of pristine graphene, making it an ideal system in which to study the electronic and magnetic interplay between local magnetic moments and Dirac electrons. These results establish a solid basis for such future studies, for example, dealing with ferromagnetism and Kondo physics in magnetically doped 2D materials. Although this work deals with Mn doping of graphene, our approach is compatible with virtually any dopant element and any 2D material host.

METHODS

CVD Growth of Graphene. Precut and polished 2 in. Czochralski grown sapphire wafers (Roditi International Corporation) diced along the *c*-plane are used to prepare Al_2O_3 template wafers. The monocrystalline wafers have a surface misorientation smaller than 0.3°. The wafers were cleaned prior to Cu sputtering in a 3:1 concentrated acid mixture of H_2O_4:H_3PO_4 at 200 °C for 20 min followed by a UPW rinse for 3 min. Cleaned sapphire wafers are placed in a Nimbus 310 sputtering setup with a base pressure of 4×10^{-6} mbar. Substrates are placed using a 200 mm Si pocket wafer, and sputtering is performed at room temperature for 173 s (21 passes under target) at 6×10^{-3} mbar Ar pressure. The Cu deposition rate is calibrated and corresponds to a rate of about 29 Å s^{-1}. The applied power was 3000 W, and the throw distance is approximately 50 mm. The graphene growth process has been optimized, taking into account oriented monolayer growth and a low Raman D peak. The growth conditions are 5000 sccm Ar: 125 sccm H_2: 0.3 sccm CH_4 at a pressure of 750 mbar close to the melting point of Cu. The growth time is 30 min, while ramp up and down is performed in a mixture of Ar and H_2.

Scanning Tunneling Microscopy. The STM micrographs reported here were obtained in UHV (base pressure $\sim 10^{-11}$ mbar) at low temperatures (2, 5, and 78 K) using an Omicron LT STM and an Unisoku USM-1500. We used electrochemically etched W tips and cut Pt−Ir tips. The tip oxide from the W tips is first removed by flash annealing. Both types of tips were characterized by scanning the Au(111) surface. All topographies were acquired in constant $I_{tun.}$.

X-ray Photoelectron Spectroscopy. XPS measurements were performed at the SuperESCA beamline at Elettra synchrotron in Trieste. All the spectra were acquired in UHV (base pressure $\sim 10^{-10}$mbar) and at room temperature, the samples were placed in the normal emission configuration, with respect to the hemispherical analyzer. The samples were annealed *in situ* up to 700 °C, with a ramp rate of 1 °C/s to monitor the change of Mn concentration. The C 1s, O 1s, and Mn 2p core-level spectra were acquired at photon energies of 400, 650, and 780 eV, respectively. The core-level spectra were fitted with Doniach−Šunjić functions convoluted with a Gaussian distribution and a linear background (apart from Mn 2p core-level, where a Shirley background is used).

Raman Spectroscopy. Raman spectra were measured using a confocal Raman microscope (Monovista CRS+, S&I GmbH) equipped with a 532 nm Nd:YAG laser. The laser was directed onto the sample surface through an objective (OLYMPUS, BX43 100× , N.A. 0.7), with the maximum laser power remaining below 1 mW in order to avoid laser-induced modification. All the measurements were obtained in ambient conditions at room temperature.

Angle-Resolved Photoemission Spectroscopy. ARPES measurements were performed at the BaDElPh beamline at Elettra synchrotron in Trieste,[46] with a photon energy of 34 eV. Before the measurements, the sample was preannealed at 700 °C. The ARPES spectra were obtained in UHV (base pressure $\sim 5 \times 10^{-11}$mbar) at 80 K. The presented spectra correspond to a summation of data that were separately acquired using linear p- and s-polarized light. The energy and angular resolution were set to 10 meV and 0.1°, respectively.

Low-Energy Electron Diffraction. As-grown graphene samples were characterized using low-energy electron diffraction (LEED) measured in an UHV chamber with background pressure better than 4×10^{-9}mbar using a rear-view AEP 8011, VG Scientific instrument. LEED images were recorded using the screen voltage and an electron beam (spot size ca. 1 mm) energy of 1 kV and 52 eV, respectively.

Density Functional Theory Calculations. We performed density functional theory calculations with generalized gradient approximation for the exchange−correlation potential, using a localized orbital basis set and a pseudopotential description of the core electrons, as implemented in the SIESTA code. In the adopted model, graphene is matched to the underlying Cu(111) surface, by taking the theoretical lattice constant (a_{theo} = 3.59 Å), resulting in a 3% expansion of the overlayer. We considered one defect related to Mn implantation in a (7 × 7) supercell, corresponding to a Mn−C ratio of 1/97−1%. Instead of dealing with Moiré reconstruction that would require a very large periodicity, we separately analyze different possible stacking configurations, corresponding to different high-symmetry regions of the Moiré, placing the Mn atom in different positions with respect to the graphene lattice and the underlying substrate. This choice is supported by the local nature of the graphene−Mn−Cu interaction in proximity of the defect, leading to electronic, magnetic, and structural properties that are not dependent on the long-range arrangement typical of the Moiré. We performed structural relaxation of the overlayer with the Mn atom, while the Cu is taken as fixed to the relaxed coordinate of the surface. The threshold for the force tolerance was set to 0.04 eV/Å. We adopted a mesh cutoff of 450 Ry and a 5 × 5 × 1 sampling of the Brillouin zone. Along the direction perpendicular to the surface, three layers of Cu were considered for structural relaxation, while a six layer Cu slab was adopted for the evaluation of the electronic properties. The periodic replica of the system along the same direction were separated by a 40 Å wide vacuum region.

The STM simulations were performed in a Tersoff−Hamann approach,[47] assuming a constant density of states for the tip. The integration range for the electronic density, corresponding to the applied bias, was varied in an energy interval of 1.0 eV around the Fermi level. We simulated a constant-height (3 Å) STM image applying a Gaussian spatial broadening of 1 Å to the electronic density to mimic the finite experimental resolution associated with the tip.

ASSOCIATED CONTENT

Supporting Information

The Supporting Information is available free of charge at https://pubs.acs.org/doi/10.1021/acsnano.1c00139.

Additional results from the DFT calculations and from the experimental studies (PDF)

AUTHOR INFORMATION

Corresponding Authors

Renan Villarreal − *Quantum Solid State Physics, KU Leuven, 3001 Leuven, Belgium;* orcid.org/0000-0003-2162-7083; Email: renan.villarreal@kuleuven.be

Lino M. C. Pereira − *Quantum Solid State Physics, KU Leuven, 3001 Leuven, Belgium*; Email: lino.pereira@kuleuven.be

Authors

Pin-Cheng Lin − *Quantum Solid State Physics, KU Leuven, 3001 Leuven, Belgium;* orcid.org/0000-0001-8355-5084

https://dx.doi.org/10.1021/acsnano.1c00139
ACS Nano 2021, 15, 5449−5458

Simona Achilli − *ETSF and Dipartimento di Fisica "Aldo Pontremoli", Università degli Studi di Milano, I-20133 Milano, Italy;* orcid.org/0000-0001-6812-5043
Harsh Bana − *Quantum Solid State Physics, KU Leuven, 3001 Leuven, Belgium;* orcid.org/0000-0003-0722-1319
Maya N. Nair − *CUNY Advanced Science Research Center, New York 10031, United States*
Antonio Tejeda − *Laboratoire de Physique des Solides, CNRS, Université Paris-Sud, 91405 Orsay, France;* orcid.org/0000-0003-0125-4603
Ken Verguts − *imec vzw, 3001 Leuven, Belgium; Department of Chemistry, Division of Molecular Design and Synthesis, KU Leuven, 3001 Leuven, Belgium*
Stefan De Gendt − *imec vzw, 3001 Leuven, Belgium; Department of Chemistry, Division of Molecular Design and Synthesis, KU Leuven, 3001 Leuven, Belgium*
Manuel Auge − *II.Institute of Physics, University of Göttingen, 37077 Göttingen, Germany*
Hans Hofsäss − *II.Institute of Physics, University of Göttingen, 37077 Göttingen, Germany*
Steven De Feyter − *Department of Chemistry, Division of Molecular Imaging and Photonics, KU Leuven, 3001 Leuven, Belgium;* orcid.org/0000-0002-0909-9292
Giovanni Di Santo − *Elettra Sincrotrone Trieste, 34149 Trieste, Italy;* orcid.org/0000-0001-9394-2563
Luca Petaccia − *Elettra Sincrotrone Trieste, 34149 Trieste, Italy;* orcid.org/0000-0001-8698-1468
Steven Brems − *imec vzw, 3001 Leuven, Belgium*
Guido Fratesi − *ETSF and Dipartimento di Fisica "Aldo Pontremoli", Università degli Studi di Milano, I-20133 Milano, Italy;* orcid.org/0000-0003-1077-7596

Complete contact information is available at: https://pubs.acs.org/10.1021/acsnano.1c00139

Author Contributions

◆P.-C.L. and R.V. contributed equally to this work.

Notes

The authors declare no competing financial interest.

ACKNOWLEDGMENTS

This work was funded by KU Leuven and FWO Vlaanderen. M.N.N. acknowledges funding from the EU Horizon 2020 Framework (MagDirac project, ID:796940). K.V. also acknowledges funding from the Agency for Innovation and Entrepreneurship (VLAIO). The authors acknowledge Elettra Sincrotrone Trieste for providing access to its synchrotron radiation facilities and, in particular, to the BaDElPh and SuperESCA beamlines as well as the Red Espanola de Supercomputacion (RES) for the availability of high-performance computing resources and support under the project FI-2020-2-0034. The authors thank P. Lacovig and S. Lizzit for the support during the XPS beam time at SuperESCA, Elettra. The authors also thank P. Walke for the support with the Raman spectroscopy measurements.

REFERENCES

(1) Jiang, Y.; Lo, P.-W.; May, D.; Li, G.; Guo, G.-Y.; Anders, F. B.; Taniguchi, T.; Watanabe, K.; Mao, J.; Andrei, E. Y. Inducing Kondo Screening of Vacancy Magnetic Moments in Graphene with Gating and Local Curvature. *Nat. Commun.* **2018**, *9*, 2349.
(2) González-Herrero, H.; Gómez-Rodríguez, J. M.; Mallet, P.; Moaied, M.; Palacios, J. J.; Salgado, C.; Ugeda, M. M.; Veuillen, J.-Y.; Yndurain, F.; Brihuega, I. Atomic-Scale Control of Graphene Magnetism by Using Hydrogen Atoms. *Science* **2016**, *352*, 437−441.
(3) Ren, J.; Guo, H.; Pan, J.; Zhang, Y. Y.; Wu, X.; Luo, H.-G.; Du, S.; Pantelides, S. T.; Gao, H.-J. Kondo Effect of Cobalt Adatoms on a Graphene Monolayer Controlled by Substrate-Induced Ripples. *Nano Lett.* **2014**, *14*, 4011−4015.
(4) Baltic, R.; Donati, F.; Singha, A.; Wäckerlin, C.; Dreiser, J.; Delley, B.; Pivetta, M.; Rusponi, S.; Brune, H. Magnetic Properties of Single Rare-Earth Atoms on Graphene/Ir (111). *Phys. Rev. B: Condens. Matter Mater. Phys.* **2018**, *98*, 024412.
(5) Ajejas, F.; Gudin, A.; Guerrero, R.; Anadon Barcelona, A.; Diez, J. M.; de Melo Costa, L.; Olleros, P.; Nino, M. A.; Pizzini, S.; Vogel, J.; Valvidares, M.; Gargiani, P.; Cabero, M.; Varela, M.; Camarero, J.; Miranda, R.; Perna, P. Unraveling Dzyaloshinskii-Moriya Interaction and Chiral Nature of Graphene/Cobalt Interface. *Nano Lett.* **2018**, *18*, 5364−5372.
(6) Candini, A.; Klyatskaya, S.; Ruben, M.; Wernsdorfer, W.; Affronte, M. Graphene Spintronic Devices with Molecular Nanomagnets. *Nano Lett.* **2011**, *11*, 2634−2639.
(7) Babar, R.; Kabir, M. Ferromagnetism in Nitrogen-Doped Graphene. *Phys. Rev. B: Condens. Matter Mater. Phys.* **2019**, *99*, 115442.
(8) Ren, J.; Guo, H.; Pan, J.; Zhang, Y.-F.; Yang, Y.; Wu, X.; Du, S.; Ouyang, M.; Gao, H.-J. Interatomic Spin Coupling in Manganese Clusters Registered on Graphene. *Phys. Rev. Lett.* **2017**, *119*, 176806.
(9) del Castillo, E.; Cargnoni, F.; Achilli, S.; Tantardini, G.; Trioni, M. Spin Asymmetric Band Gap Opening in Graphene by Fe Adsorption. *Surf. Sci.* **2015**, *634*, 62−67.
(10) del Castillo, E.; Achilli, S.; Cargnoni, F.; Ceresoli, D.; Soave, R.; Trioni, M. Spin-Filtering in Graphene Junctions with Ti and Co Adsorbates. *Chem. Phys.* **2016**, *478*, 91.
(11) Wang, H.; Wang, Q.; Cheng, Y.; Li, K.; Yao, Y.; Zhang, Q.; Dong, C.; Wang, P.; Schwingenschlogl, U.; Yang, W.; Zhang, X. Doping Monolayer Graphene with Single Atom Substitutions. *Nano Lett.* **2012**, *12*, 141−144.
(12) Robertson, A. W.; Montanari, B.; He, K.; Kim, J.; Allen, C. S.; Wu, Y. A.; Olivier, J.; Neethling, J.; Harrison, N.; Kirkland, A. I.; Warner, J. H. Dynamics of Single Fe Atoms in Graphene Vacancies. *Nano Lett.* **2013**, *13*, 1468−1475.
(13) Zhao, L.; He, R.; Rim, K. T.; Schiros, T.; Kim, K. S.; Zhou, H.; Gutierrez, C.; Chockalingam, S. P.; Arguello, C. J.; Palova, L.; Nordlund, D.; Hybertsen, M. S.; Reichman, D. R.; Heinz, T. F.; Kim, P.; Pinczuk, A.; Flynn, G. W.; Pasupathy, A. N. Visualizing Individual Nitrogen Dopants in Monolayer Graphene. *Science* **2011**, *333*, 999−1003.
(14) Terrones, H.; Lv, R.; Terrones, M.; Dresselhaus, M. S. The Role of Defects and Doping in 2D Graphene Sheets and 1D Nanoribbons. *Rep. Prog. Phys.* **2012**, *75*, 062501.
(15) Zhou, W.; Kapetanakis, M. D.; Prange, M. P.; Pantelides, S. T.; Pennycook, S. J.; Idrobo, J.-C. Direct Determination of the Chemical Bonding of Individual Impurities in Graphene. *Phys. Rev. Lett.* **2012**, *109*, 206803.
(16) Ramasse, Q. M.; Seabourne, C. R.; Kepaptsoglou, D.-M.; Zan, R.; Bangert, U.; Scott, A. J. Probing the Bonding and Electronic Structure of Single Atom Dopants in Graphene with Electron Energy Loss Spectroscopy. *Nano Lett.* **2013**, *13*, 4989−4995.
(17) Susi, T.; Meyer, J. C.; Kotakoski, J. Manipulating Low-Dimensional Materials down to the Level of Single Atoms with Electron Irradiation. *Ultramicroscopy* **2017**, *180*, 163−172.
(18) Dyck, O.; Zhang, L.; Yoon, M.; Swett, J. L.; Hensley, D.; Zhang, C.; Rack, P. D.; Fowlkes, J. D.; Lupini, A. R.; Jesse, S. Doping Transition-Metal Atoms in Graphene for Atomic-Scale Tailoring of Electronic, Magnetic, and Quantum Topological Properties. *Carbon* **2021**, *173*, 205−214.
(19) Bangert, U.; Pierce, W.; Kepaptsoglou, D.; Ramasse, Q.; Zan, R.; Gass, M.; van den Berg, J.; Boothroyd, C.; Amani, J.; Hofsäss, H. Ion Implantation of Graphene - Toward IC Compatible Technologies. *Nano Lett.* **2013**, *13*, 4902−4907.

(20) Willke, P.; Amani, J.; Thakur, S.; Weikert, S.; Druga, T.; Maiti, K.; Hofsäss, H.; Wenderoth, M. Short-Range Ordering of Ion-Implanted Nitrogen Atoms in SiC-Graphene. *Appl. Phys. Lett.* **2014**, *105*, 111605.
(21) Kepaptsoglou, D.; Hardcastle, T. P.; Seabourne, C. R.; Bangert, U.; Zan, R.; Amani, J. A.; Hofsäss, H.; Nicholls, R. J.; Brydson, R. M. D.; Scott, A. J.; Ramasse, Q. M. Electronic Structure Modification of Ion Implanted Graphene: The Spectroscopic Signatures of *p*- and *n*-Type Doping. *ACS Nano* **2015**, *9*, 11398−11407.
(22) Willke, P.; Amani, J. A.; Sinterhauf, A.; Thakur, S.; Kotzott, T.; Druga, T.; Weikert, S.; Maiti, K.; Hofsäss, H.; Wenderoth, M. Doping of Graphene by Low-Energy Ion Beam Implantation: Structural, Electronic, and Transport Properties. *Nano Lett.* **2015**, *15*, 5110−5115.
(23) Cress, C. D.; Schmucker, S. W.; Friedman, A. L.; Dev, P.; Culbertson, J. C.; Lyding, J. W.; Robinson, J. T. Nitrogen-Doped Graphene and Twisted Bilayer Graphene via Hyperthermal Ion Implantation with Depth Control. *ACS Nano* **2016**, *10*, 3714−3722.
(24) Susi, T.; Hardcastle, T. P.; Hofsäss, H.; Mittelberger, A.; Pennycook, T. J.; Mangler, C.; Drummond-Brydson, R.; Scott, A. J.; Meyer, J. C.; Kotakoski, J. Single-Atom Spectroscopy of Phosphorus Dopants Implanted into Graphene. *2D Mater.* **2017**, *4*, 021013.
(25) Tripathi, M.; Markevich, A.; Bottger, R.; Facsko, S.; Besley, E.; Kotakoski, J.; Susi, T. Implanting Germanium into Graphene. *ACS Nano* **2018**, *12*, 4641−4647.
(26) Krasheninnikov, A.; Lehtinen, P.; Foster, A. S.; Pyykkö, P.; Nieminen, R. M. Embedding Transition-Metal Atoms in Graphene: Structure, Bonding, and Magnetism. *Phys. Rev. Lett.* **2009**, *102*, 126807.
(27) Verguts, K.; Vermeulen, B.; Vrancken, N.; Schouteden, K.; Van Haesendonck, C.; Huyghebaert, C.; Heyns, M.; De Gendt, S.; Brems, S. Epitaxial Al2O3(0001)/Cu(111) Template Development for CVD Graphene Growth. *J. Phys. Chem. C* **2016**, *120*, 297−304.
(28) Gottardi, S.; Müller, K.; Bignardi, L.; Moreno-López, J. C.; Pham, T. A.; Ivashenko, O.; Yablonskikh, M.; Barinov, A.; Björk, J.; Rudolf, P.; Stöhr, M. Comparing Graphene Growth on Cu(111) versus Oxidized Cu(111). *Nano Lett.* **2015**, *15*, 917−922.
(29) Khomyakov, P.; Giovannetti, G.; Rusu, P.; Brocks, G. v.; van den Brink, J.; Kelly, P. J. First-Principles Study of the Interaction and Charge Transfer between Graphene and Metals. *Phys. Rev. B: Condens. Matter Mater. Phys.* **2009**, *79*, 195425.
(30) Drummond, T. J. Work Functions of the Transition Metals and Metal Silicides; *Report no. SAND99-0391J*; U.S. Department of Energy: Washington, DC, 1999.
(31) Avila, J.; Razado, I.; Lorcy, S.; Fleurier, R.; Pichonat, E.; Vignaud, D.; Wallart, X.; Asensio, M. C. Exploring Electronic Structure of One-Atom Thick Polycrystalline Graphene Films: A Nano Angle Resolved Photoemission Study. *Sci. Rep.* **2013**, *3*, 2439.
(32) Vita, H.; Böttcher, S.; Horn, K.; Voloshina, E.; Ovcharenko, R.; Kampen, T.; Thissen, A.; Dedkov, Y. S. Understanding the Origin of Band Gap Formation in Graphene on Metals: Graphene on Cu/Ir (111). *Sci. Rep.* **2015**, *4*, 5704.
(33) Alford, T. L.; Feldman, L. C.; Mayer, J. W. *Fundamentals of Nanoscale Film Analysis*; Springer Science & Business Media: Boston, MA, 2007.
(34) Meyer, J. C.; Eder, F.; Kurasch, S.; Skakalova, V.; Kotakoski, J.; Park, H. J.; Roth, S.; Chuvilin, A.; Eyhusen, S.; Benner, G.; Krasheninnikov, A. V.; Kaiser, U. Accurate Measurement of Electron Beam Induced Displacement Cross Sections for Single-Layer Graphene. *Phys. Rev. Lett.* **2012**, *108*, 196102.
(35) Rodriguez-Manzo, J. A.; Cretu, O.; Banhart, F. Trapping of Metal Atoms in Vacancies of Carbon Nanotubes and Graphene. *ACS Nano* **2010**, *4*, 3422−3428.
(36) Chen, J.-H.; Li, L.; Cullen, W. G.; Williams, E. D.; Fuhrer, M. S. Tunable Kondo Effect in Graphene with Defects. *Nat. Phys.* **2011**, *7*, 535−538.
(37) Liang, L.; Costa Girao, E.; Meunier, V. Modeling the Kondo Effect of a Magnetic Atom Adsorbed on Graphene. *2D Mater.* **2019**, *6*, 035038.
(38) Jacob, D. Towards a Full ab Initio Theory of Strong Electronic Correlations in Nanoscale Devices. *J. Phys.: Condens. Matter* **2015**, *27*, 245606.
(39) Choi, T. Studies of Single Atom Magnets via Scanning Tunneling Microscopy. *J. Magn. Magn. Mater.* **2019**, *481*, 150−155.
(40) Girovsky, J.; Nowakowski, J.; Ali, M. E.; Baljozovic, M.; Rossmann, H. R.; Nijs, T.; Aeby, E. A.; Nowakowska, S.; Siewert, D.; Srivastava, G.; Wackerlin, C.; Dreiser, J.; Decurtins, S.; Liu, S.-X.; Oppeneer, P. M.; Jung, T. A.; Ballav, N. Long-Range Ferrimagnetic Order in a Two-Dimensional Supramolecular Kondo Lattice. *Nat. Commun.* **2017**, *8*, 15388.
(41) Joly, L.; Kappler, J.-P.; Ohresser, P.; Sainctavit, P.; Henry, Y.; Gautier, F.; Schmerber, G.; Kim, D.; Goyhenex, C.; Bulou, H.; Bengone, O.; Kavich, J.; Gambardella, P.; Scheurer, F. Kondo Screening of the Spin and Orbital Magnetic Moments of Fe Impurities in Cu. *Phys. Rev. B: Condens. Matter Mater. Phys.* **2017**, *95*, 041108.
(42) Mo, S.-K. Angle-Resolved Photoemission Spectroscopy for the Study of Two-Dimensional Materials. *Nano Convergence* **2017**, *4*, 6.
(43) Singh, N.; Schwingenschlögl, U. A Route to Permanent Valley Polarization in Monolayer MoS2. *Adv. Mater.* **2017**, *29*, 1600970.
(44) Tran, T. T.; Bray, K.; Ford, M. J.; Toth, M.; Aharonovich, I. Quantum Emission from Hexagonal Boron Nitride Monolayers. *Nat. Nanotechnol.* **2016**, *11*, 37−41.
(45) Castelletto, S.; Inam, F. A.; Sato, S.-i.; Boretti, A. Hexagonal Boron Nitride: A Review of the Emerging Material Platform for Single-Photon Sources and the Spin-Photon Interface. *Beilstein J. Nanotechnol.* **2020**, *11*, 740−769.
(46) Petaccia, L.; Vilmercati, P.; Gorovikov, S.; Barnaba, M.; Bianco, A.; Cocco, D.; Masciovecchio, C.; Goldoni, A. BaD ElPh: A 4 m Normal-Incidence Monochromator Beamline at Elettra. *Nucl. Instrum. Methods Phys. Res., Sect. A* **2009**, *606*, 780−784.
(47) Tersoff, J.; Hamann, D. R. Theory of the Scanning Tunneling Microscope. *Phys. Rev. B: Condens. Matter Mater. Phys.* **1985**, *31*, 805.

https://dx.doi.org/10.1021/acsnano.1c00139
ACS Nano 2021, 15, 5449−5458